Electronic Supplementary Information

Self-Supported FeCoNiCuP High-Entropy Alloy Nanosheet Arrays for Efficient Glycerol Oxidation and Hydrogen Evolution in Seawater Electrolyte

Leyang Song,[a,b] Chaoqun Ma,[c] Peidong Shi,[a,b] Xiaojuan Zhu,[a,b] Kaiyu Qu,[a,b] Lijie Zhu,[d,*] Qipeng Lu,[c,*] and An-Liang Wang[a,b,*]

[a]Key Laboratory for Colloid and Interface Chemistry Ministry of Education, State Key Laboratory of Crystal Materials, School of Chemistry and Chemical Engineering, Shandong University. Jinan, 250100, Shandong, China.

[b]Suzhou Research Institute, Shandong University, Suzhou, 215123, Jiangsu, China.

[c]School of Materials Science and Engineering, University of Science and Technology Beijing, Beijing, 100083, China.

[d]School of Instrument Science and Opto-Electronics Engineering, Beijing Information Science and Technology University, Beijing, 100192, China.

[*]Corresponding author.

Email: ljzhu@bistu.edu.cn; qipeng@ustb.edu.cn; alwang@sdu.edu.cn.

Experimental Section

Chemicals

Copper sulfate pentahydrate ($CuSO_4·5H_2O$, 99%), iron (II) sulfate heptahydrate ($FeSO_4·7H_2O$, 99%), nickel sulfate hexahydrate ($NiSO_4·6H_2O$, 98.5%), boric acid (H_3BO_3, 99.5%), ammonium chloride (NH_4Cl, 99.5%), ethyl alcohol (C_2H_6O, 99.7%), nitric acid (HNO_3, 30%), sulfuric acid (H_2SO_4, 98%) and glycerol ($C_3H_8O_3$, 99%) were purchased from Sinopharm Chemical Reagent Co., Ltd. Hydrochloric acid (HCl, 36-38 wt%) was purchased from Laiyang Kangde Chemical Co., Ltd. Sodium hypophosphite (NaH_2PO_2, 99%), cobalt chloride hexahydrate ($CoCl_2·6H_2O$, 99.9%), potassium hydroxide (KOH, 90%), and glyceric acid ($C_3H_6O_4$, 95%) were purchased from Shanghai Macklin Biochemical Co., Ltd. Glyceraldehyde ($C_3H_6O_3$, 90%) was purchased from J&K Scientific Chemical Reagent Co., Ltd. Glycolic acid ($C_2H_4O_3$, 99%) was purchased from Shanghai Deb Biotechnology Co., Ltd. Formic acid (CH_2O_2, 99%) was purchased from Shanghai Adamas Reagent Co., Ltd. Nafion solution (5 wt%) was obtained from Dupont. Pt/C (20%) was bought from Suzhou Yilongsheng Energy Technology Co., Ltd. Seawater used in the experiment was collected from the Yellow Sea (Weihai, China). All chemicals were used without further purification. Carbon cloth (CC) was purchased from Suzhou Sinero Technology Co., Ltd.

Synthesis of FeCoNiCuP high entropy alloy nanosheet arrays (HEANAs)

The carbon cloth (CC, 1 × 2 cm^2) was rinsed with water and ethanol, respectively. The electrodeposition was carried out in a two-electrode cell by galvanostatic electrolysis. The CC was used as the working electrode and carbon rod serves as the counter electrode. The FeCoNiCuP HEANAs were electrodeposited on the surface of CC in the solution of 45.0 mM $NiSO_4·6H_2O$ + 10.0 mM $CuSO_4·5H_2O$ + 25.0 mM $CoCl_2·6H_2O$ + 25.0 mM $FeSO_4·7H_2O$ + 200.0 mM NaH_2PO_2 + 20.0 mM H_3BO_3 + 25.0 mM NH_4Cl for 10 min at room temperature at the cathodic current density of 50 mA cm^{-2}. In addition, the FeCoNiCuP samples with different proportions were synthesized by only changing the content of electrodeposition solutions. The electrodeposition solution of 25.0 mM $NiSO_4·6H_2O$ + 20.0 mM $CuSO_4·5H_2O$ + 25.0 mM $CoCl_2·6H_2O$ + 25.0 mM $FeSO_4·7H_2O$ was used to synthesize FeCoNiCuP-2. FeCoNiCuP-3 was electrodeposited in the solution of 50.0 mM $NiSO_4·6H_2O$ + 10.0 mM $CuSO_4·5H_2O$ + 25.0 mM $CoCl_2·6H_2O$ + 25.0 mM $FeSO_4·7H_2O$. The electrodeposition solution of 50.0 mM $NiSO_4·6H_2O$ + 10.0 mM $CuSO_4·5H_2O$ + 50.0

mM $CoCl_2 \cdot 6H_2O$ + 25.0 mM $FeSO_4 \cdot 7H_2O$ was utilized to synthesize FeCoNiCuP-4. The electrodeposition solution of 25.0 mM $NiSO_4 \cdot 6H_2O$ + 10.0 mM $CuSO_4 \cdot 5H_2O$ + 25.0 mM $CoCl_2 \cdot 6H_2O$ + 50.0 mM $FeSO_4 \cdot 7H_2O$ was used to synthesize FeCoNiCuP-5.

Synthesis of CoNiCuP nanosheet arrays (NAs)

The synthesis procedure of CoNiCuP NAs was similar as that of FeCoNiCuP HEANAs except that $FeSO_4 \cdot 7H_2O$ was not added.

Synthesis of FeNiCuP NAs

The synthesis procedure of FeNiCuP NAs was similar as that of FeCoNiCuP HEANAs except that $CoCl_2 \cdot 6H_2O$ was not added.

Synthesis of FeCoCuP NAs

The synthesis procedure of FeCoCuP NAs was similar as that of FeCoNiCuP HEANAs except that $NiSO_4 \cdot 6H_2O$ was not added.

Synthesis of FeCoNiP NAs

The synthesis procedure of FeCoNiP NAs was similar as that of FeCoNiCuP HEANAs except that $CuSO_4 \cdot 5H_2O$ was not added.

Synthesis of FeCoNiCu NAs

The synthesis procedure of FeCoNiCu NAs was similar as that of FeCoNiCuP HEANAs except that NaH_2PO_2 was not added.

Material characterizations

Powder X-ray diffraction (XRD, Rigaku SmartLab) with Cu Kα radiation source (λ = 1.5418 Å) was used to characterize the crystalline phase of all catalysts. The morphologies of catalysts were investigated using scanning electron microscope (SEM, JEOL JSM-7800F) and transmission electron microscope (TEM, HITACHI 7700). The high-resolution transmission electron microscope (HRTEM) and energy dispersive X-ray spectrometer mapping (EDS-mapping) were recorded on JEOL 2100F. X-ray photoelectron spectroscopy (XPS) measurements were carried out on an ESCALAB 250Xi instrument and the data was calibrated using C 1s peak at 284.8 eV. The inductively coupled plasma-atomic emission spectroscopy (ICP-AES) was performed on an Agilent 730 ES. The ultraviolet-visible (UV-vis) absorbance spectra were collected on SHIMADZU UV-1900 spectrophotometer. ^{1}H nuclear magnetic resonance (^{1}H NMR) measurements were recorded on a 400 MHz Bruker Avance spectrometer. The products from the electrochemical oxidation of glycerol were detected by high performance liquid chromatography (HPLC, Primaide).

Electrochemical measurements

All electrochemical tests were carried out in a standard three-electrode cell system on an electrochemical workstation (CHI 760E, Shanghai Chenhua Co., Ltd) at room temperature. CC with as-prepared catalysts was used as the working electrode (mass loading of catalyst: 0.8 mg cm^{-2}), carbon rod and Hg/HgO electrode were used as the counter electrode and the reference electrode, respectively. All potentials were calibrated by reversible hydrogen electrode (RHE) using the following equation: $E_{RHE} = E_{Hg/HgO} + 0.098 + 0.059 \times pH$. The electrochemical glycerol oxidation reaction (GOR) tests were carried out in Ar-saturated 1.0 M KOH aqueous solution with 0.1 M glycerol. For the electrochemical tests analyzing the oxidation of GOR intermediates, 0.1 M of respective molecule was added to the electrolyte. All polarization curves were obtained with iR compensation at a scan rate of 10 mV s^{-1}. The electrochemical impedance spectroscopy (EIS) was measured in the region of 0.1-100000 Hz. The long-term electrolysis of electrocatalysts was performed by chronopotentiometry.

The determination of Faradic efficiency of H_2

The Faradaic efficiency (FE) refers to the ratio of experimentally produced H_2 to theoretically calculated H_2, which was obtained by water drainage method. The FE (%) was calculated by the following equation:

$$FE\ (\%) = (n \times F \times V / (Q \times V_m)) \times 100\%$$

where n is the number of moles of electrons transferred when 1 mol of H_2 is produced; F is the Faraday constant (96485 C mol^{-1}); V is the gas volume; V_m is the molar volume and Q is the total electric charge.

Determination of electrochemical surface area (ECSA)

Cyclic voltammetric (CV) curves with different sweep rates (20, 40, 60, 80, 100 and 120 mV s^{-1}) were used to calculate the double-layer capacitance (C_{dl}). The current density differences ($\Delta j = j_a - j_c$) were plotted against scan rates, and the linear slope represents twice the C_{dl}. The ECSA of electrocatalysts is calculated based on the following equation:

$$ECSA = C_{dl} / C_s$$

where C_s is the specific capacitance (0.06 mF cm^{-2}) of a smooth planar surface with 1.0 cm^2 surface area.[1]

Product analysis

The oxidation products were analyzed by ^1H NMR and HPLC analysis. The chronamperometry tests at different applied potentials were carried out to determine the products and calculate the FE. For each NMR measurement, 500 μL of electrolyte

was extracted, and 100 μL D_2O with a certain amount of maleic acid ($C_4H_4O_4$) were added as internal standard for products analysis. The oxidation products were identified by analyzing the chemical shift in ^1H NMR spectra. For HPLC tests, electrolyte was initially neutralized with 0.5 M H_2SO_4 with a volume ratio of 1:1. The neutralized electrolyte was injected into an Aminex HPX-87H column (300 mm × 7.8 mm). The mobile phase was 5 mM H_2SO_4 with a flow rate of 0.6 mL min^{-1}. The determination of product concentrations was based on the calibration curves obtained from standard solutions with known concentrations. The FE (%) of formate was calculated using the following equation:

$$FE\ (\%) = (n_{(formate)} \times Z \times F / Q) \times 100\%$$

where $n_{(formate)}$ is the number of moles of formate produced; Q is the total charge transferred during the reaction, Z is 8/3, representing the number of charges transferred for the production of 1 mol of formate; and F is the Faraday constant.

The setup assembly and performance test with continuous mode

FeCoNiCuP HEANAs supported on CC were used as both cathode and anode in a continuous electrochemical reactor. The mass loading of FeCoNiCuP HEANAs was 0.8 mg cm^{-2}. The anode, cathode, anion exchange membrane (Fumasep FAA-3-PK), and bipolar plate were assembled to form the reactor. The experimental setup consisted of reactor as the core component, along with pumps, beakers, electrochemical station. The anodic compartment of the electrochemical reactor was fed with a solution containing 1 M KOH + 0.1 M glycerol and the cathodic compartment was flowed with a solution containing 1 M KOH. The experiments were performed in continuous mode and the electrolytes were pumped into the cathode and anode chambers with a single pass through a peristaltic pump (11 mL min^{-1}). The tests were carried out at ambient conditions of pressure and temperature. The chronopotentiometry tests were conducted for 1 h at the current densities of 10 mA cm^{-2} and 200 mA cm^{-2}. To measure the concentrations of oxidation products, the post-electrolyzed solution collected from the anodic chamber was neutralized with 0.5 M H_2SO_4 with a volume ratio of 1:1. The neutralized electrolyte was injected into an Aminex HPX-87H column (300 mm × 7.8 mm) for HPLC analysis. The mobile phase was 5 mM H_2SO_4 with a flow rate of 0.6 mL min^{-1}. The specific analysis and calculation methods are consistent with the methods described in the foregoing experimental section. The FE (%) of oxidation products were calculated by the following equation:

$$FE\ (\%) = (n \times Z \times F / Q) \times 100\%$$

where n is the number of moles of oxidation products; Z represents the number of charges transferred for the production of 1 mol of oxidation product (Z = 4 for glycerate, Z = 10/3 for glycolate, and Z = 8/3 for formate); F is the Faraday constant; Q is the total charge transferred during the reaction.

Density functional theory (DFT) calculations

In this study, the Vienna ab initio simulation package (VASP) was used for all calculations.[2] The interaction potential of valence electrons and core electrons was described by the projector augmented wave (PAW) method.[3] The exchange-correlation functional was processed using the Perdew-Burke-Ernzerhof (PBE) functional with the generalized gradient approximation (GGA) method.[2] All the calculations were performed in a spin-polarized manner. The plane-wave basis with cut-off energy was set to 500 eV. Additionally, the Alloy Theoretic Automated Toolkit (ATAT) was utilized to generate alloy surface models which have been employed in the special quasi-random structures (SQS) method.[4-6] In the calculations, the Brillouin zone k-point sampling was 2×2×1 Monkhorst-Pack mesh. The convergence energy threshold was set to 10^{-5} eV for electronic self-consistent iteration, and the equilibrium geometries are optimized with maximum stress on each atom within 0.05 eV/Å. The Gibbs free energy change (ΔG) of the GOR and HER was calculated with the following formula:

$$\Delta G = \Delta E + \Delta E_{ZPE} - T\Delta S$$

where ΔE is the adsorption energy of a given system, ΔE_{ZPE} represents the zero-point energy, ΔS stands for the entropy differences between the adsorbed state and the free-standing states, T is 298.15 K.

Supplementary Figures

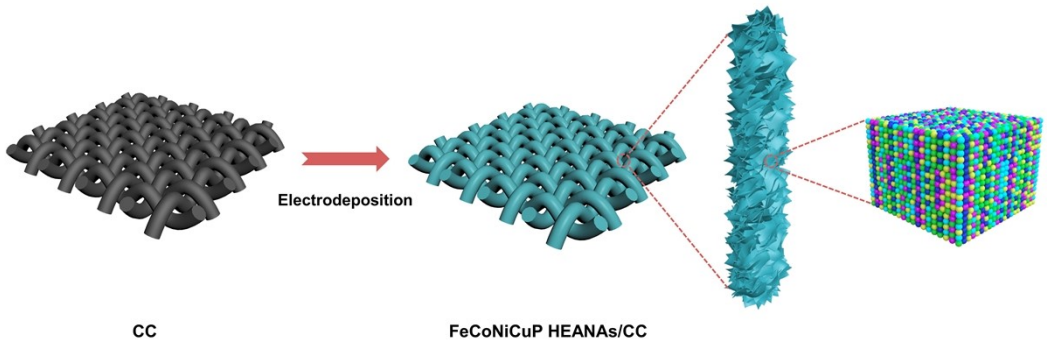

Fig. S1. Schematic illustration of the synthesis of FeCoNiCuP HEANAs on CC.

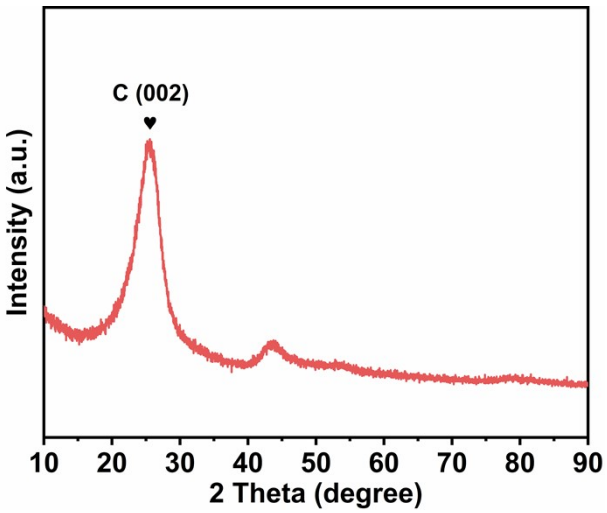

Fig. S2. The XRD pattern of carbon cloth.

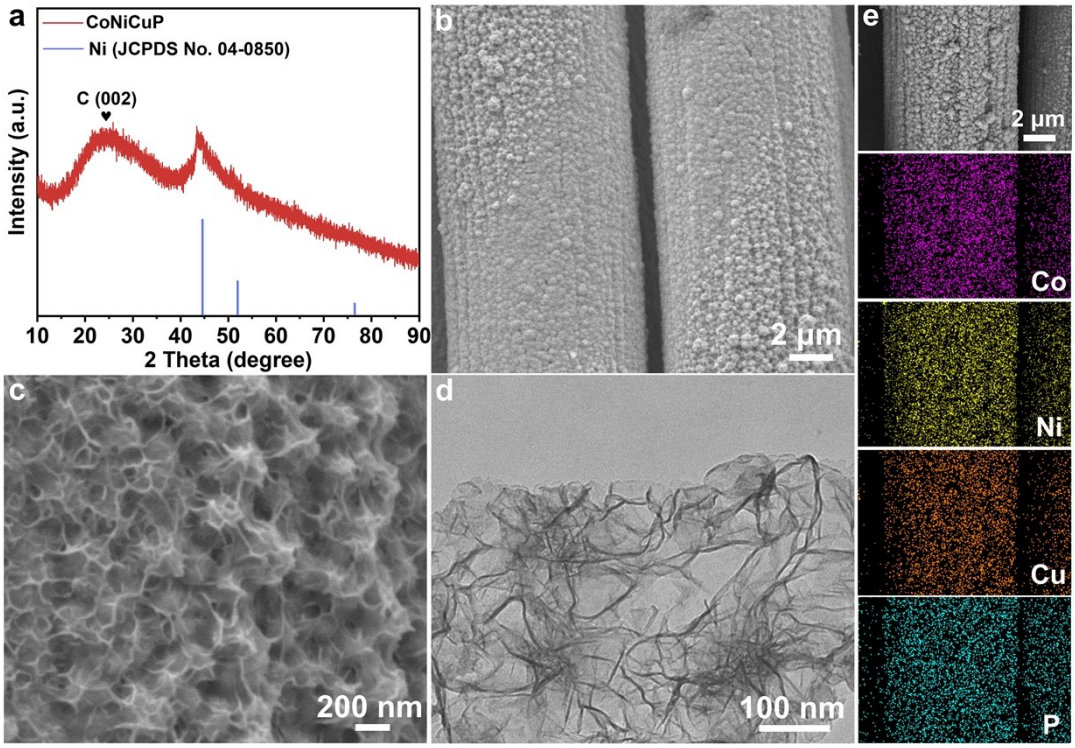

Fig. S3. (a) XRD pattern of CoNiCuP NAs/CC. (b) Low and (c) high magnification SEM images of CoNiCuP NAs on CC. (d) TEM image of CoNiCuP nanosheet. (e) SEM image of CoNiCuP NAs/CC and the corresponding elemental mappings.

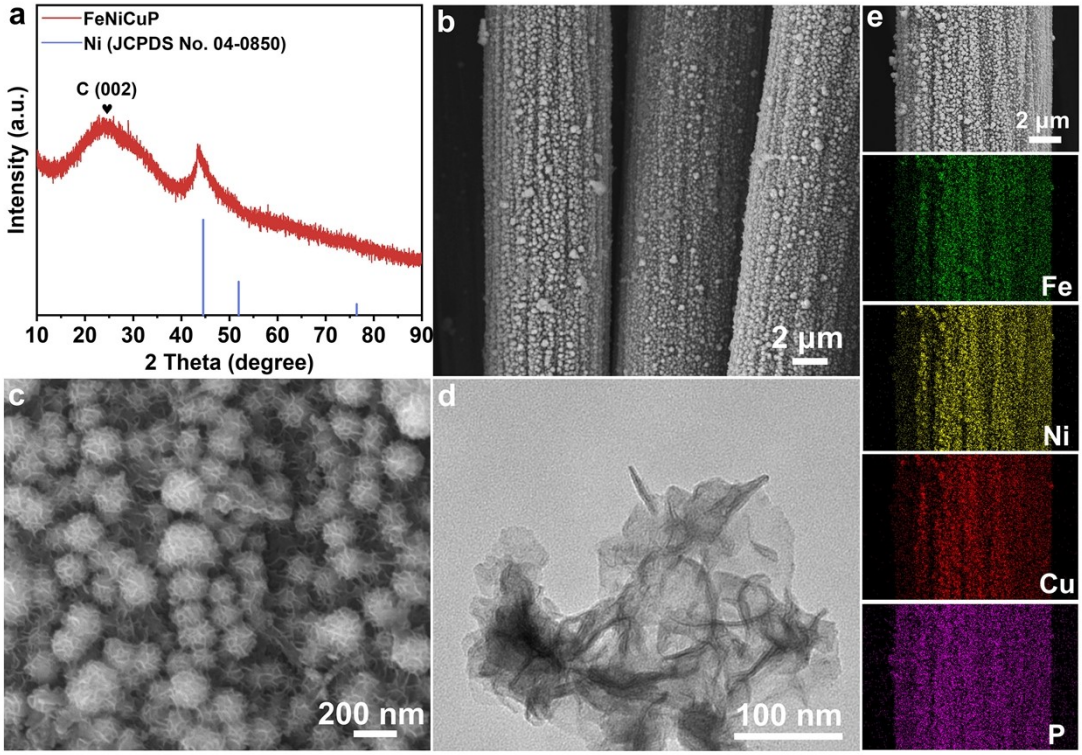

Fig. S4. (a) XRD pattern of FeNiCuP NAs/CC. (b) Low and (c) high magnification SEM images of FeNiCuP NAs on CC. (d) TEM image of FeNiCuP nanosheet. (e) SEM image of FeNiCuP NAs/CC and the corresponding elemental mappings.

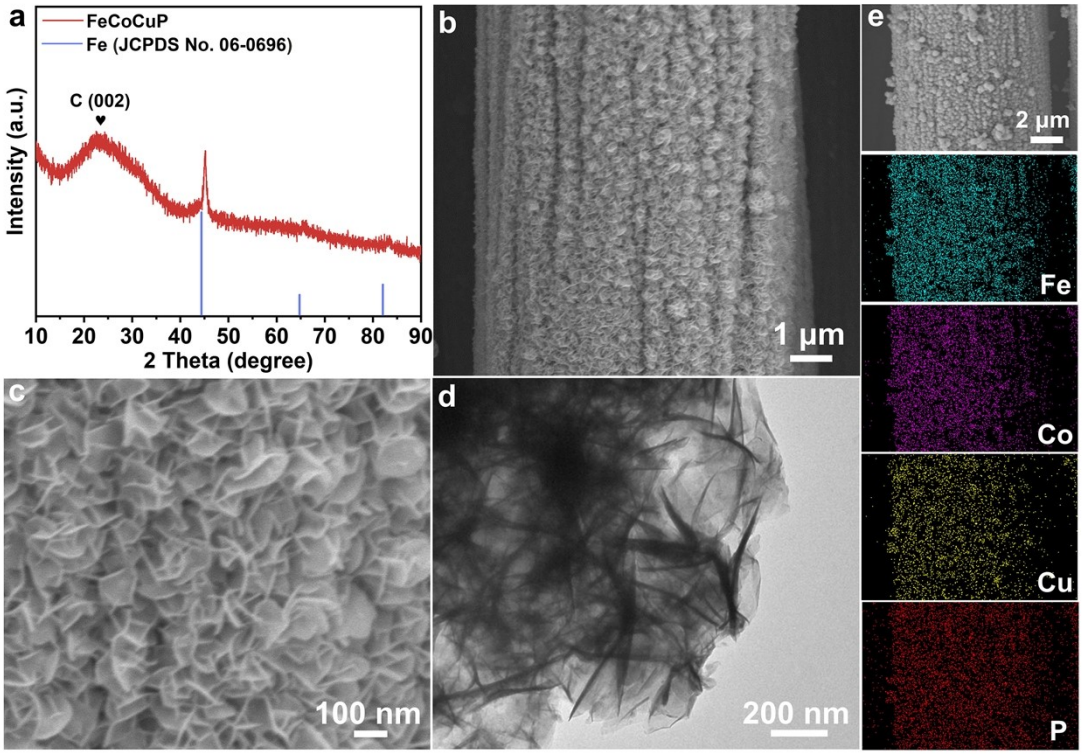

Fig. S5. (a) XRD pattern of FeCoCuP NAs/CC. (b) Low and (c) high magnification SEM images of FeCoCuP NAs on CC. (d) TEM image of FeCoCuP nanosheet. (e) SEM image of FeCoCuP NAs/CC and the corresponding elemental mappings.

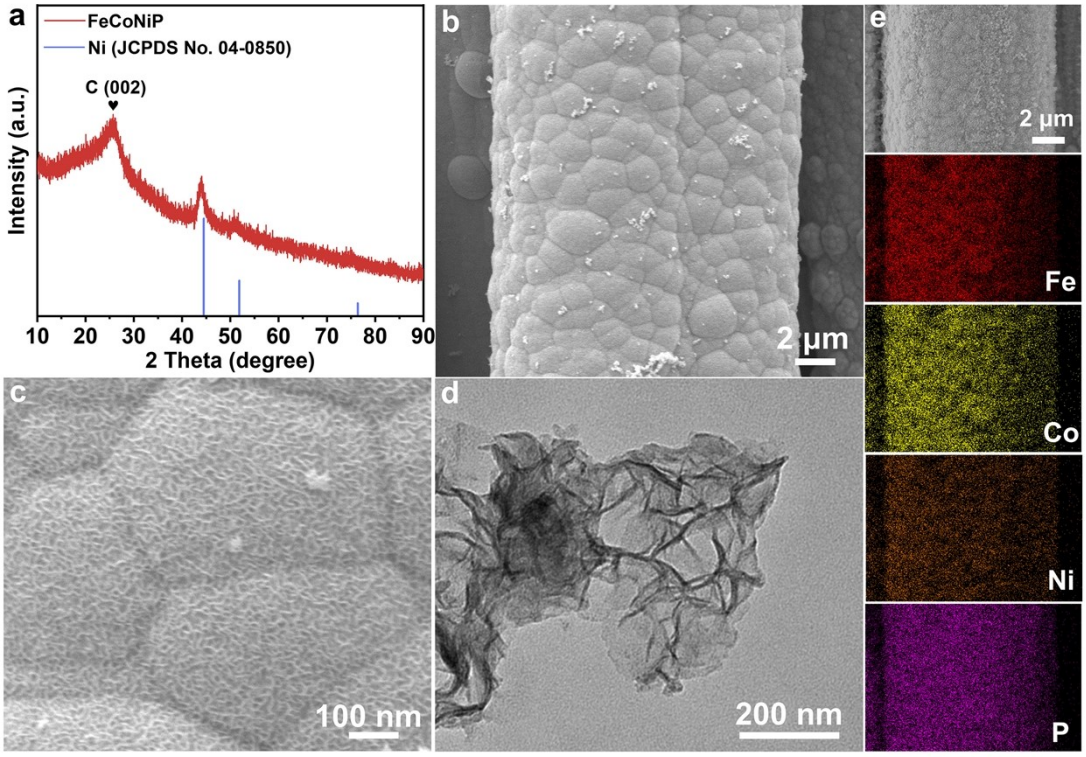

Fig. S6. (a) XRD pattern of FeCoNiP NAs/CC. (b) Low and (c) high magnification SEM images of FeCoNiP NAs on CC. (d) TEM image of FeCoNiP nanosheet. (e) SEM image of FeCoNiP NAs/CC and the corresponding elemental mappings.

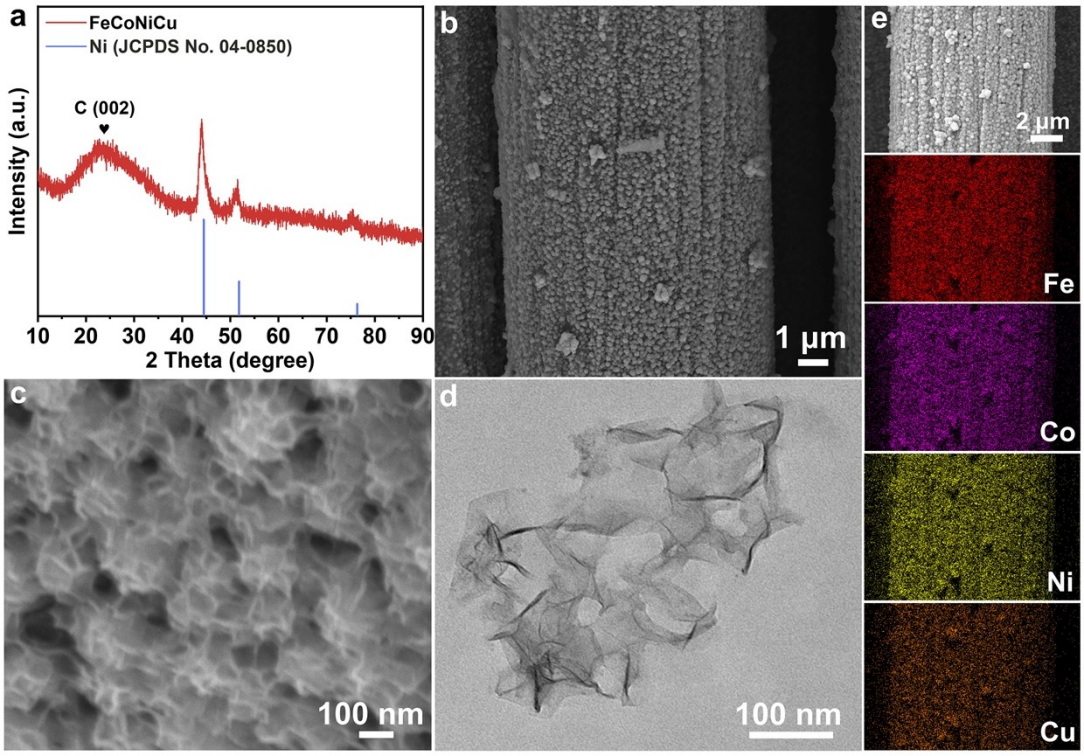

Fig. S7. (a) XRD pattern of FeCoNiCu NAs/CC. (b) Low and (c) high magnification SEM images of FeCoNiCu NAs on CC. (d) TEM image of FeCoNiCu nanosheet. (e) SEM image of FeCoNiCu NAs/CC and the corresponding elemental mappings.

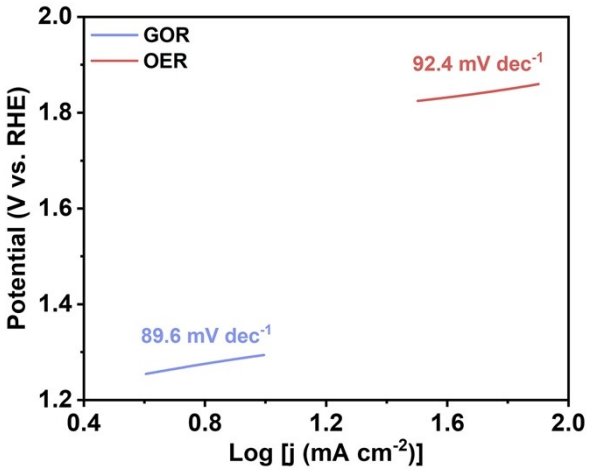

Fig. S8. Tafel slopes of FeCoNiCuP HEANAs for GOR and OER.

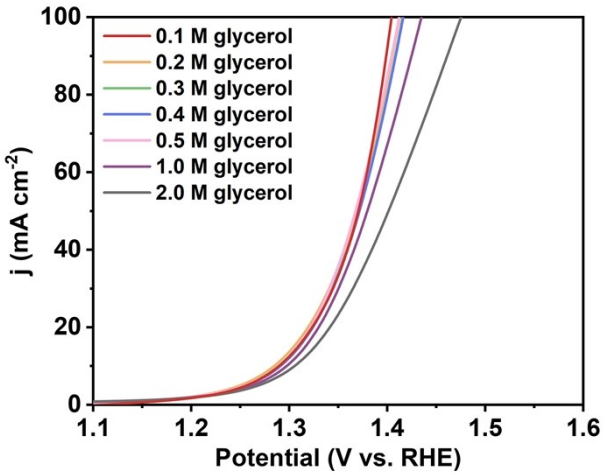

Fig. S9. Polarization curves of FeCoNiCuP HEANAs in electrolytes with different glycerol concentrations.

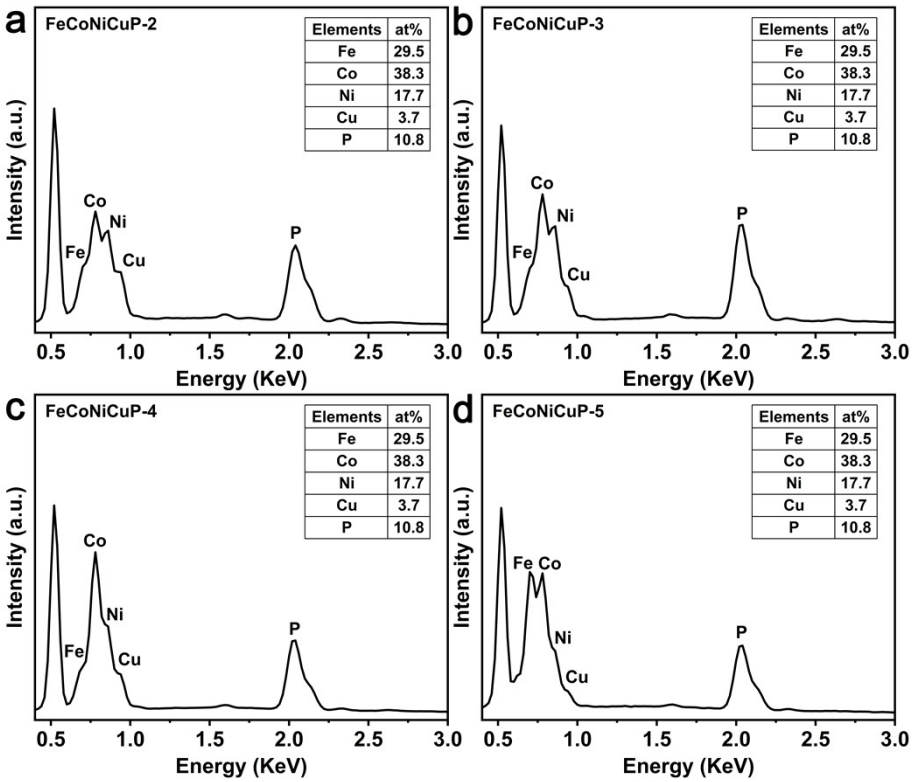

Fig. S10. The EDS results of FeCoNiCuP samples with different proportions.

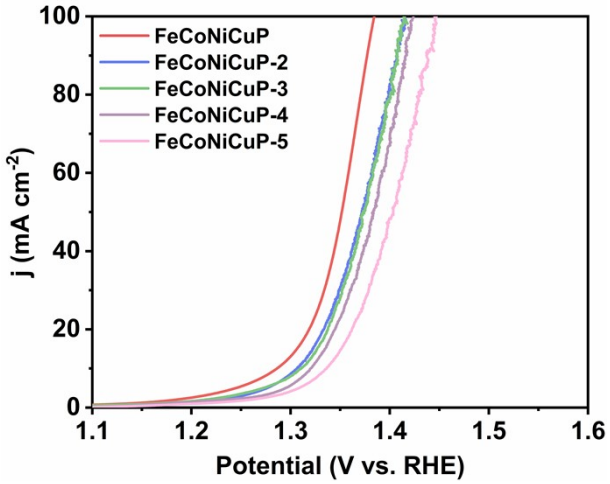

Fig. S11. Polarization curves of FeCoNiCuP samples with different proportions.

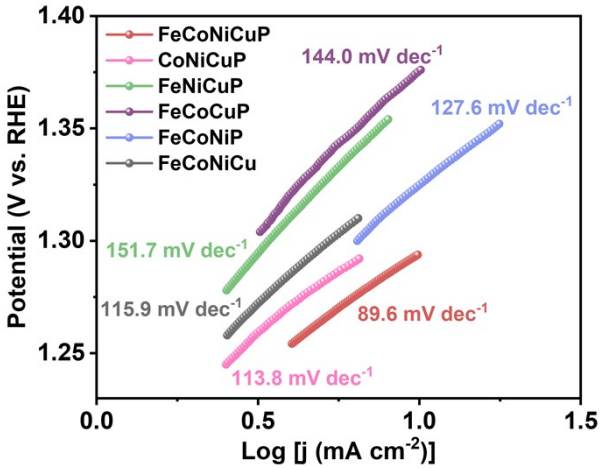

Fig. S12. Tafel slopes of FeCoNiCuP HEANAs and all quarternary alloys.

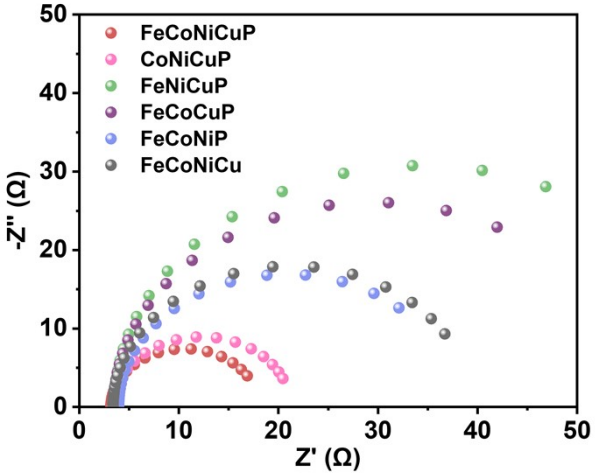

Fig. S13. EIS curves of FeCoNiCuP HEANAs and all quarternary alloys.

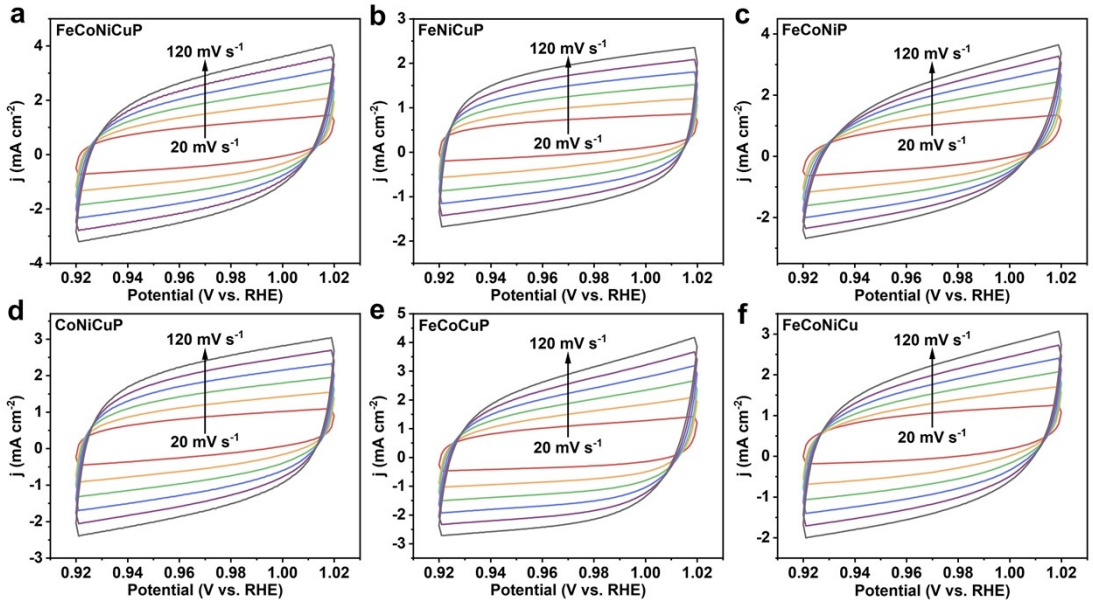

Fig. S14. (a-f) CV curves of FeCoNiCuP HEANAs and all quarternary alloys at different scan rates in 1.0 M KOH and 0.1 M glycerol.

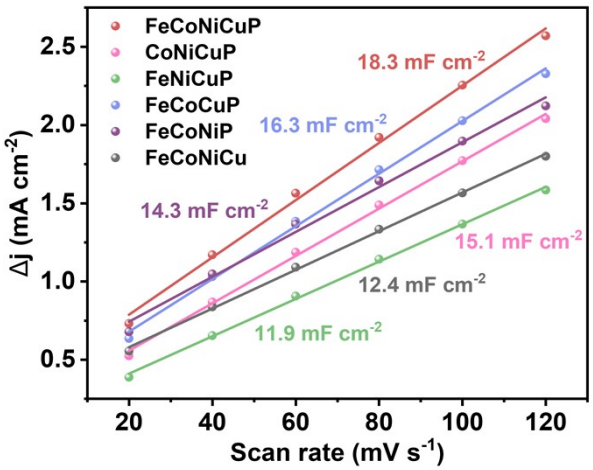

Fig. S15. The plots of capacitive current density as a function of scan rate at 0.97 V.

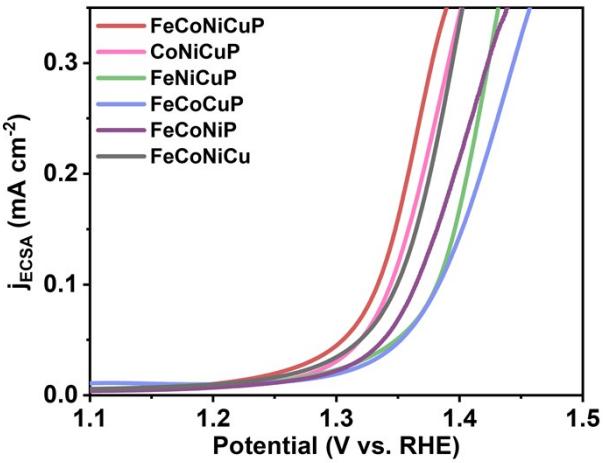

Fig. S16. The ECSA-normalized polarization curves of FeCoNiCuP HEANAs and all quarternary alloys.

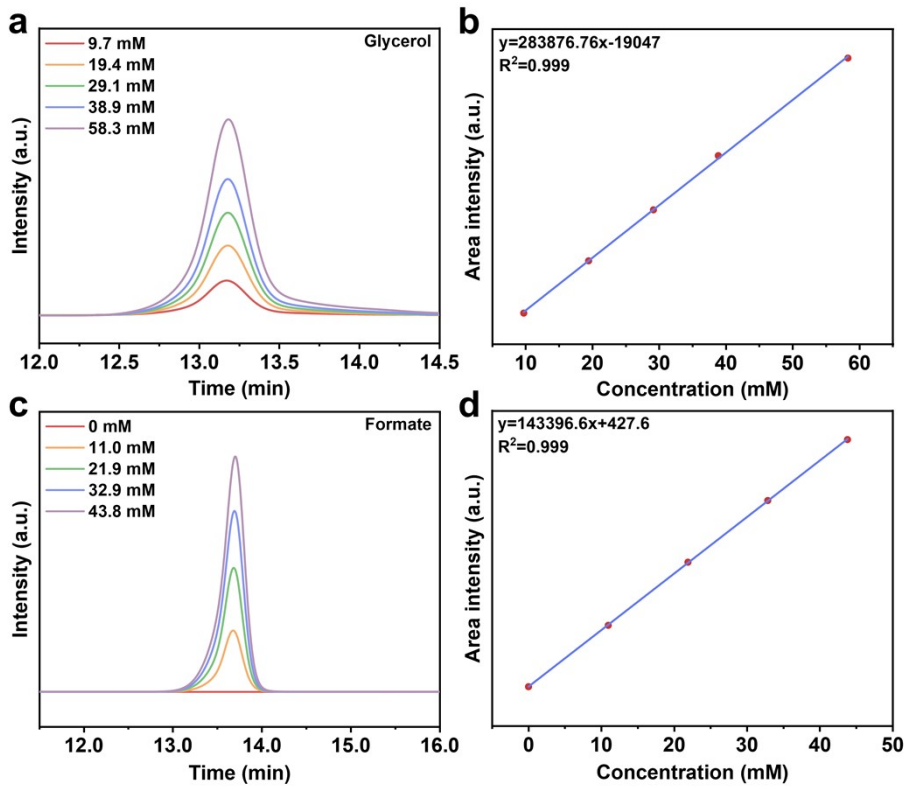

Fig. S17. Standard HPLC chromatograms of (a) glycerol and (c) formate with various concentrations. The corresponding calibration curves used to quantify the concentrations of (b) glycerol and (d) formate.

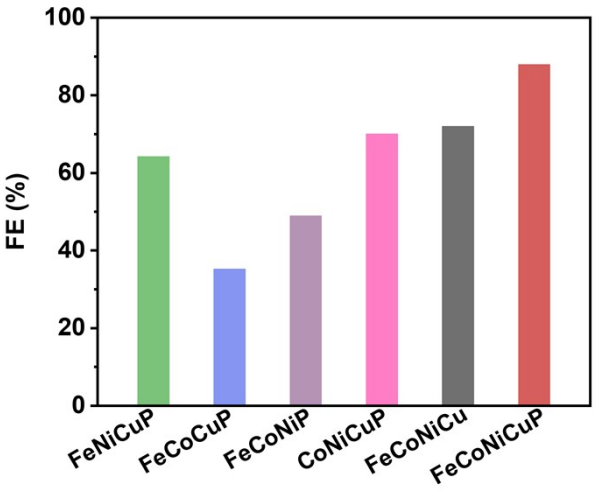

Fig. S18. The FE of FeCoNiCuP HEANAs and quaternary alloys at 1.40 V.

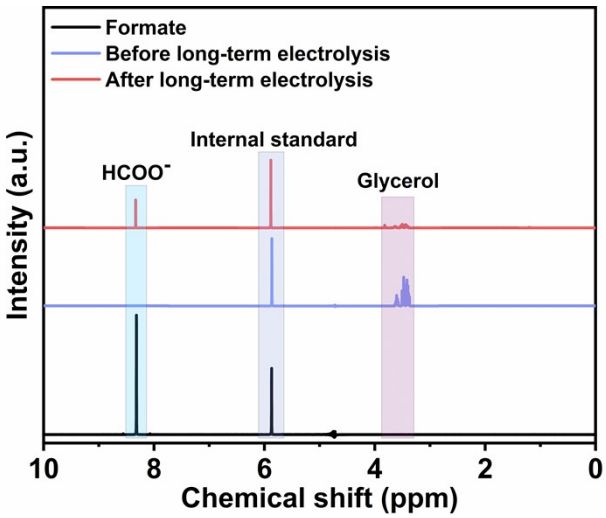

Fig. S19. ^{1}H NMR spectra of pure formate, extracted electrolytes before and after long-term electrolysis.

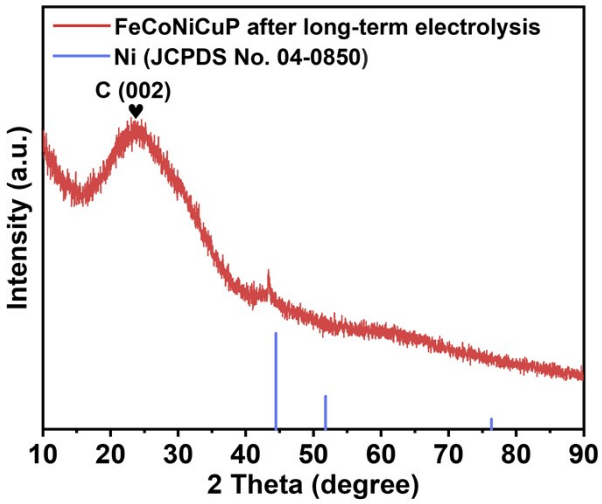

Fig. S20. XRD pattern of FeCoNiCuP HEANAs/CC after long-term electrolysis of GOR.

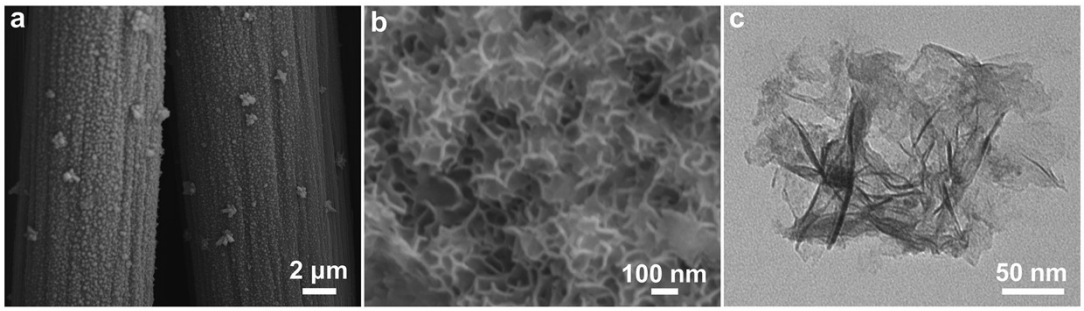

Fig. S21. The structural characterizations of FeCoNiCuP HEANAs after long-term electrolysis of GOR. (a) Low and (b) high magnification SEM images and (c) TEM image.

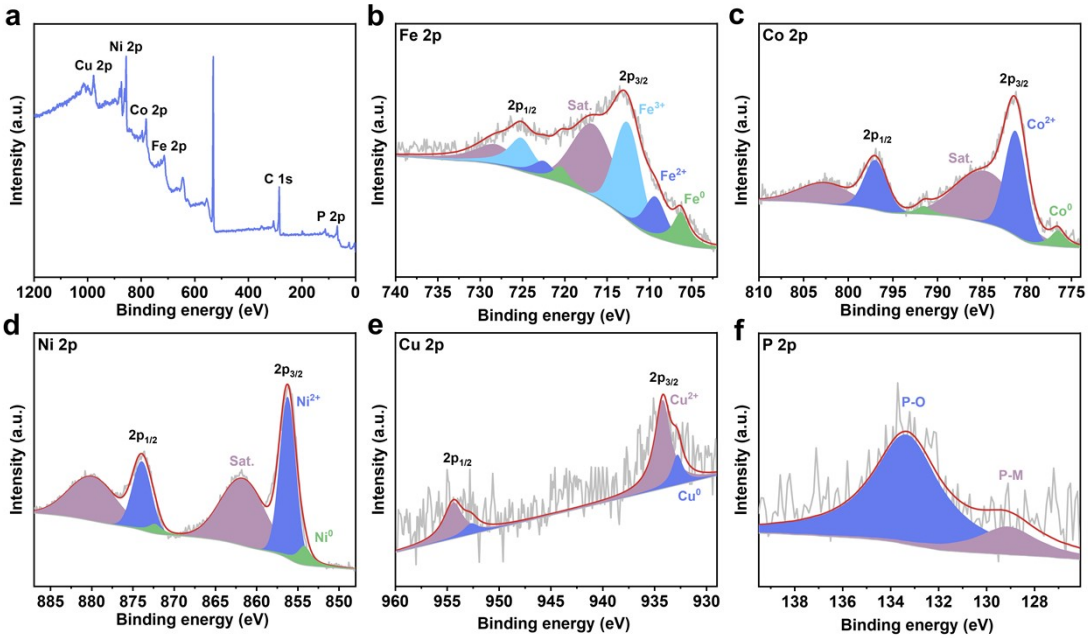

Fig. S22. XPS spectra of FeCoNiCuP HEANAs after long-term electrolysis of GOR. (a) XPS survey spectrum. High-resolution XPS spectra of (b) Fe 2p, (c) Co 2p, (d) Ni 2p, (e) Cu 2p, and (f) P 2p.

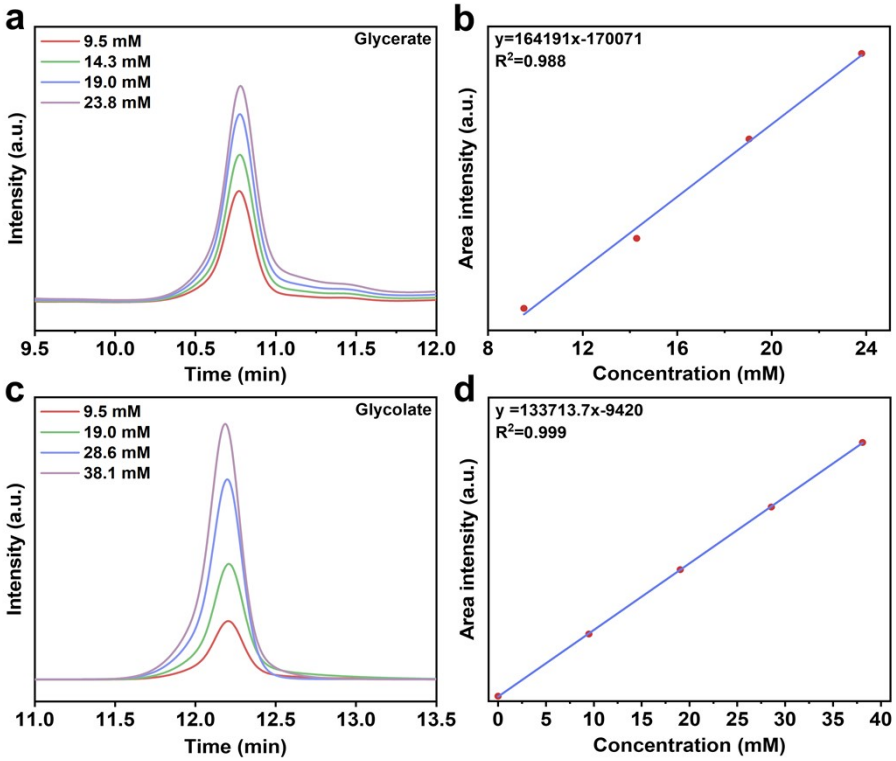

Fig. S23. Standard HPLC chromatograms of (a) glycerate and (c) glycolate with various concentrations. The corresponding calibration curves used to quantify the concentrations of (b) glycerate and (d) glycolate.

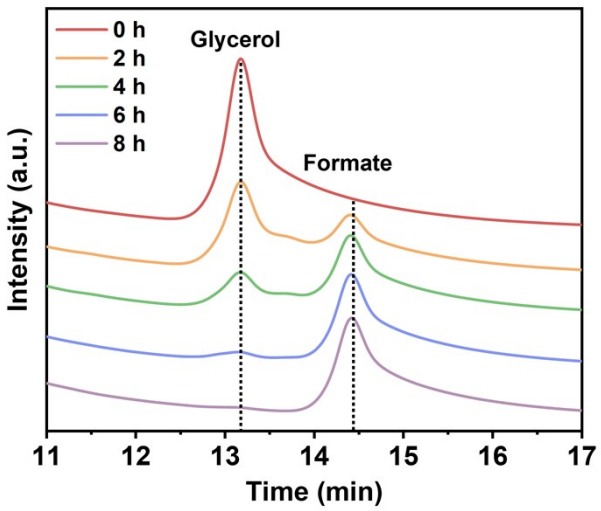

Fig. S24. HPLC chromatogram of glycerol oxidation to formate at different electrolysis time.

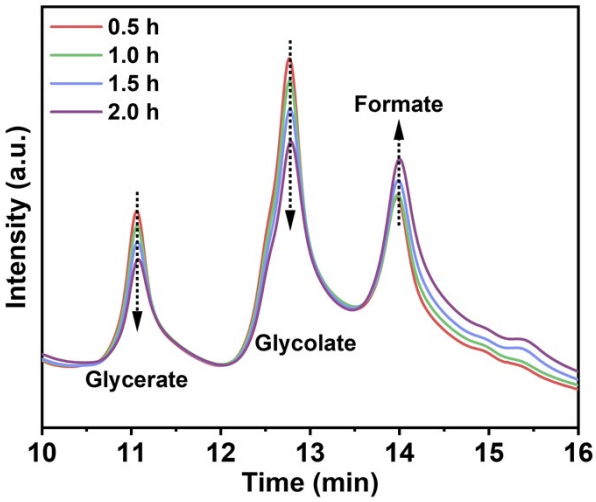

Fig. S25. HPLC chromatogram during the oxidation of glyceraldehyde at different electrolysis time.

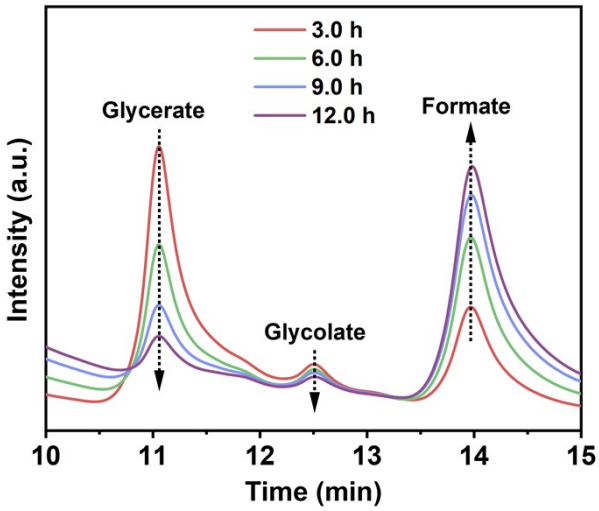

Fig. S26. HPLC chromatogram during the oxidation of glycerate at different electrolysis time.

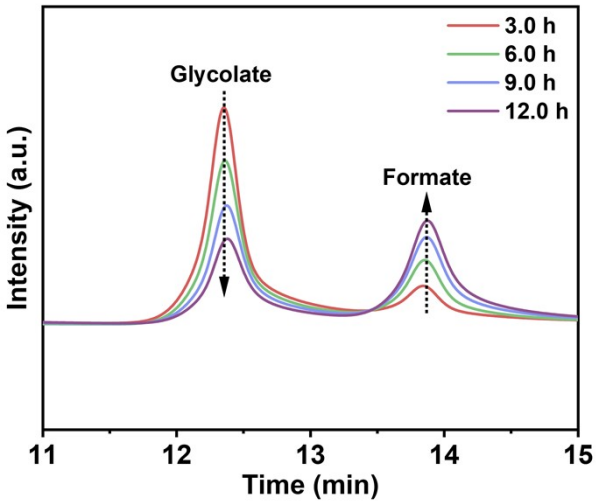

Fig. S27. HPLC chromatogram during the oxidation of glycolate at different electrolysis time.

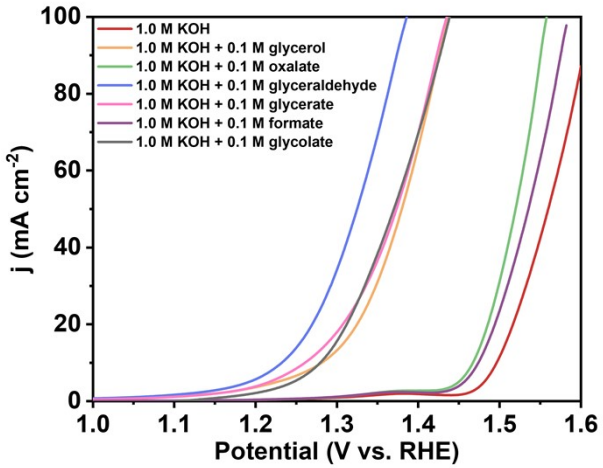

Fig. S28. Polarization curves of FeCoNiCuP HEANAs in 1.0 M KOH with 0.1 M of different molecules.

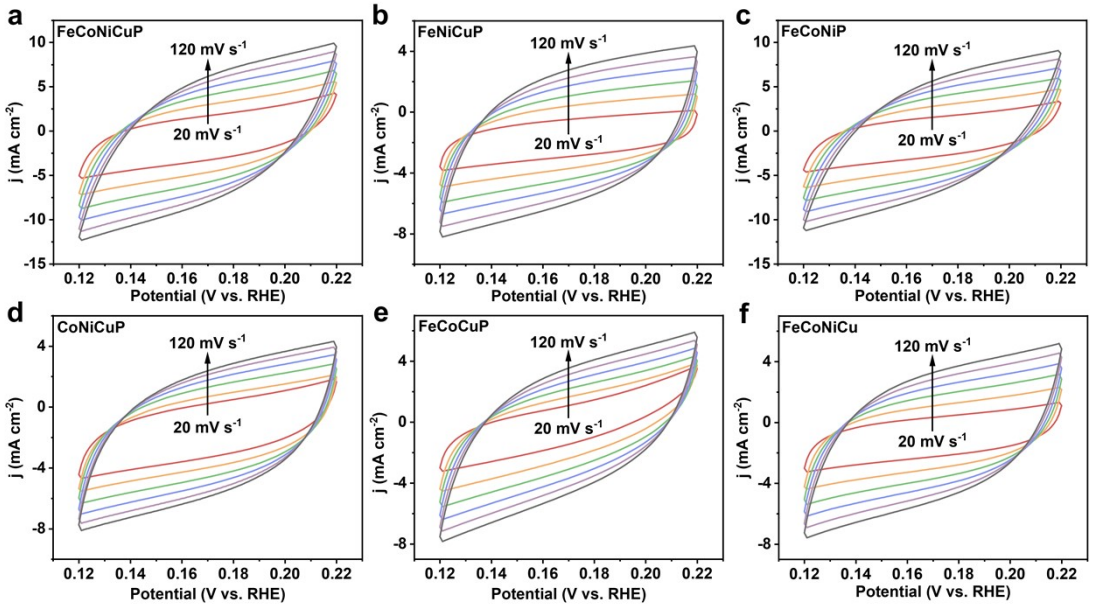

Fig. S29. (a-f) CV curves of FeCoNiCuP HEANAs and all quarternary alloys at different scan rates (20-120 mV s^{-1}) in 1.0 M KOH.

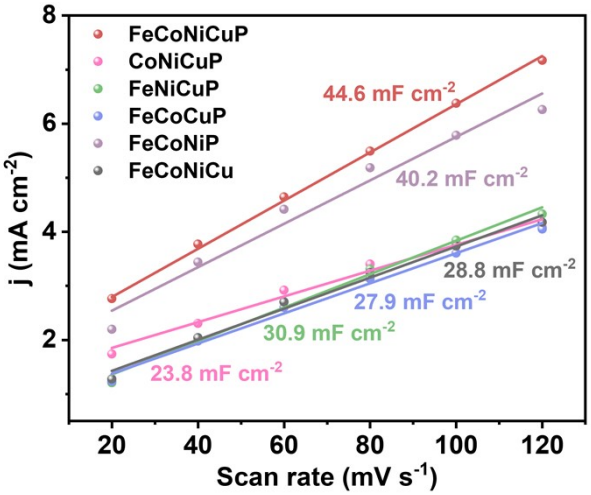

Fig. S30. The plots of capacitive current density as a function of scan rate at 0.17 V.

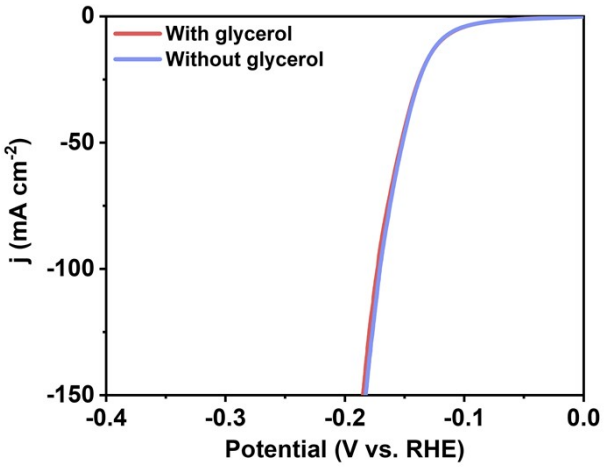

Fig. S31. HER polarization curves of FeCoNiCuP HEANAs in 1.0 M KOH with and without 0.1 M glycerol.

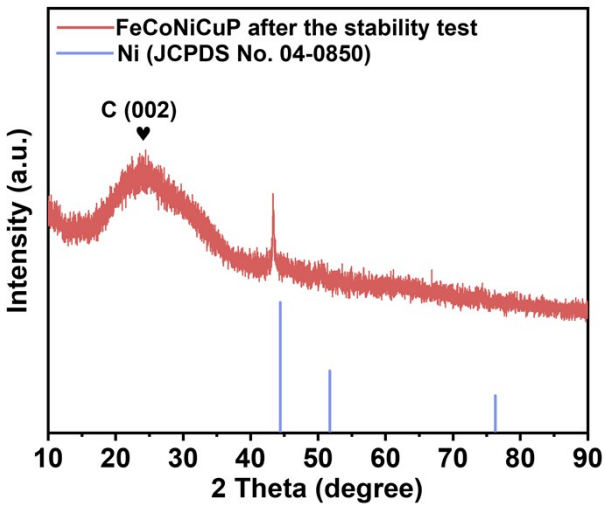

Fig. S32. The XRD pattern of FeCoNiCuP HEANAs/CC after the stability test of HER.

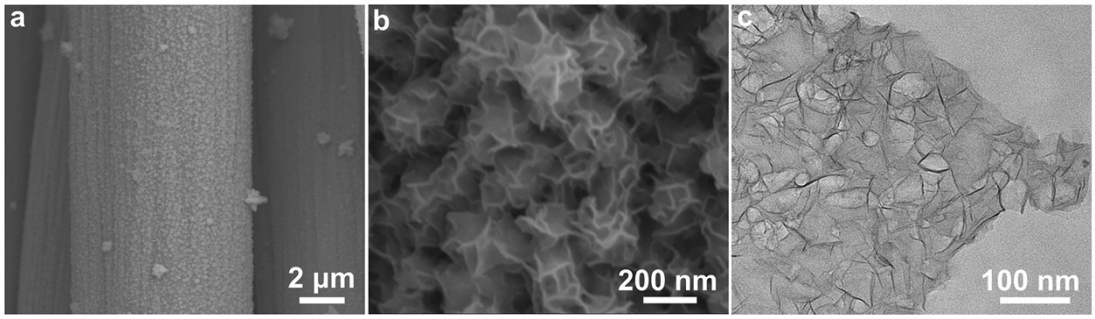

Fig. S33. The structural characterizations of FeCoNiCuP HEANAs after the stability test of HER. (a) Low and (b) high magnification SEM images and (c) TEM image.

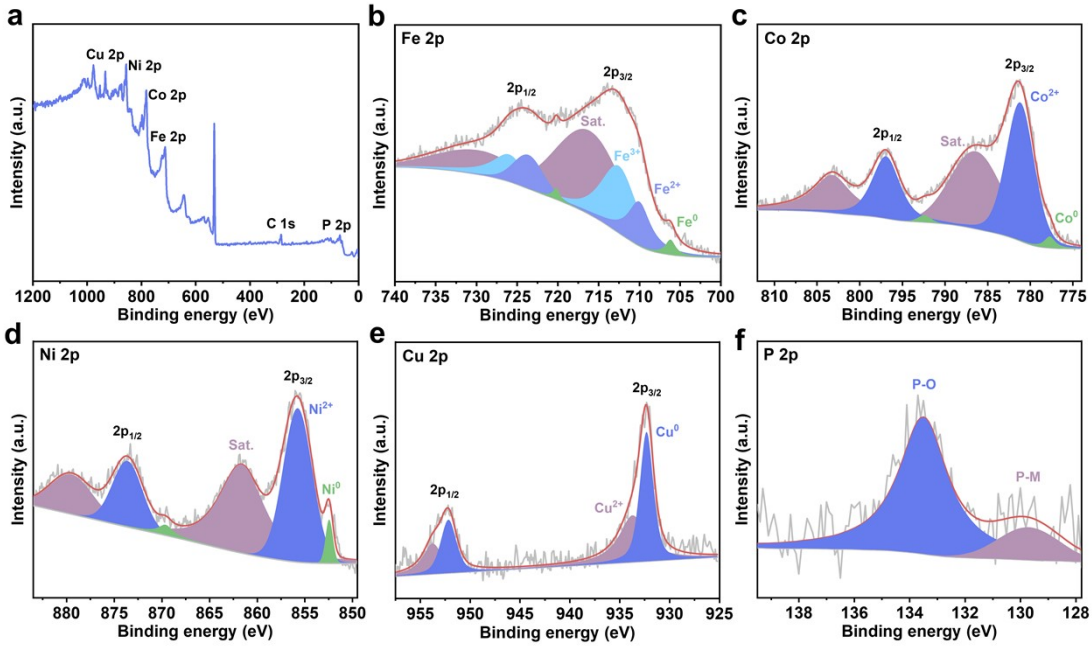

Fig. S34. XPS spectra of FeCoNiCuP HEANAs after the stability test of HER. (a) XPS survey spectrum. High-resolution XPS spectra of (b) Fe 2p, (c) Co 2p, (d) Ni 2p, (e) Cu 2p, and (f) P 2p.

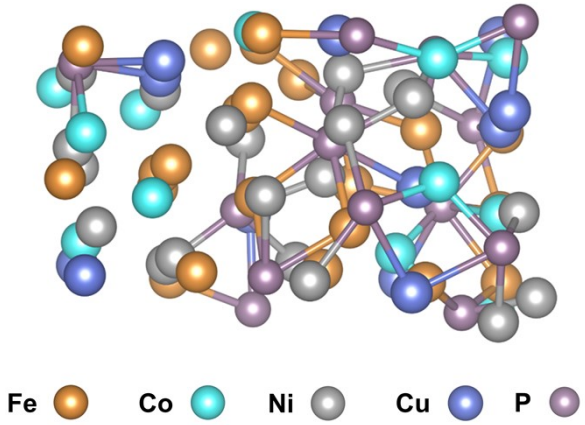

Fig. S35. Optimized structure model of FeCoNiCuP.

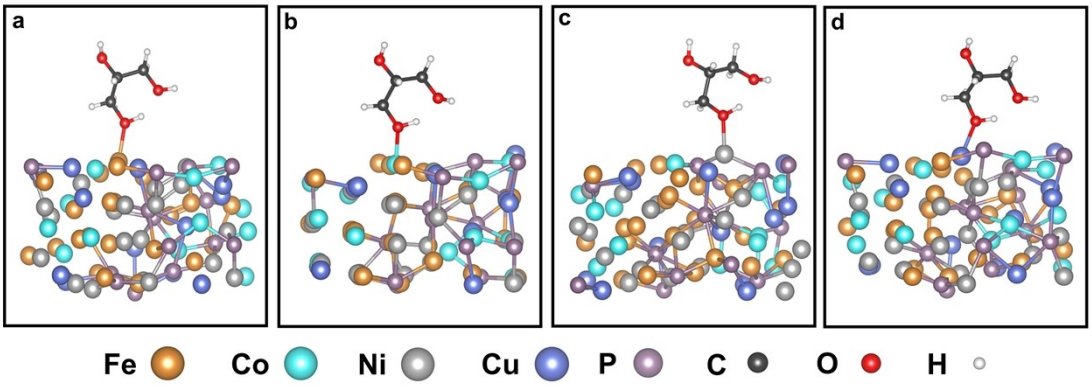

Fig. S36. Optimized structure models of glycerol molecules adsorbed on different metal sites. (a) Fe, (b) Co, (c) Ni, (d) Cu.

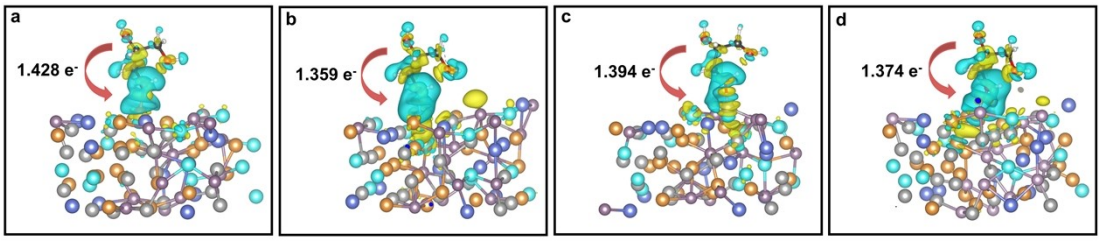

Fig. S37. Optimized structure models and charge density difference maps of glycerol molecules adsorbed on different sites in FeCoNiCuP. (a) Fe site, (b) Co site, (c) Ni site, (d) Cu site. The yellow and cyan region represent electron accumulation and electron depletion, respectively.

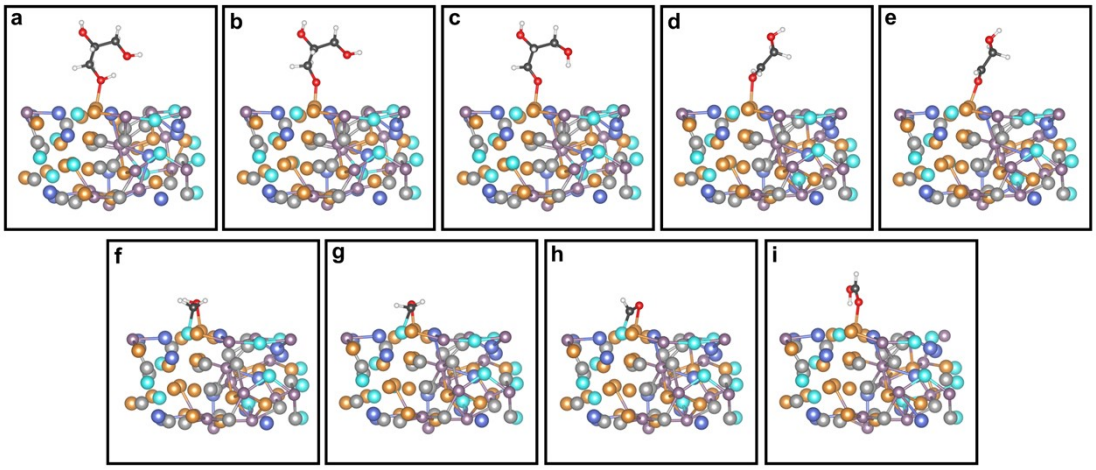

Fig. S38. Optimized structure models of FeCoNiCuP absorbed with different intermediates on Fe site. (a) *$CH_2OHCHOHCH_2OH$. (b) *$CH_2OHCHOHCH_2O$. (c) *$CH_2OHCHOHCHO$. (d) *$CH_2OHCHOH$. (e) *CH_2OHCHO. (f) *CH_2OH. (g) *CH_2O. (h) *CHO. (i) *HCOOH.

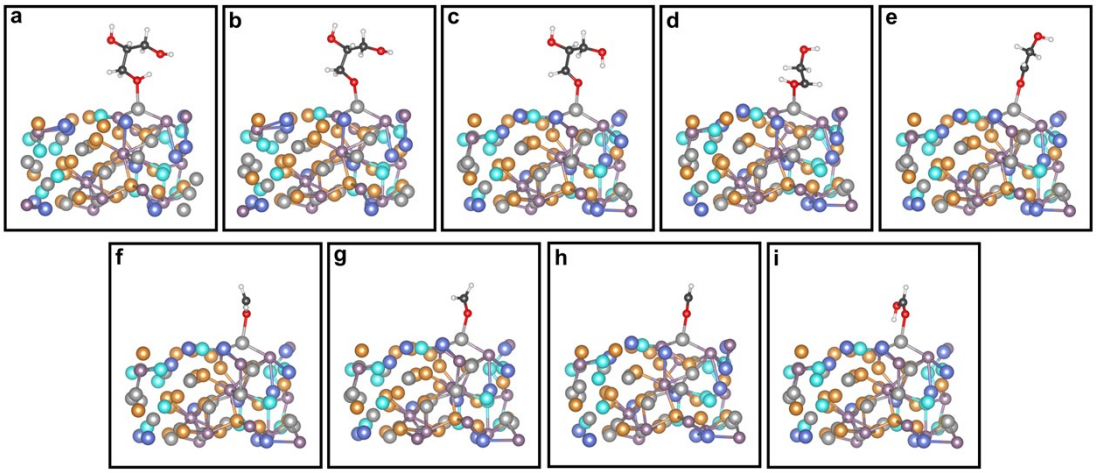

Fig. S39. Optimized structure models of FeCoNiCuP absorbed with different intermediates on Ni site. (a) *$CH_2OHCHOHCH_2OH$. (b) *$CH_2OHCHOHCH_2O$. (c) *$CH_2OHCHOHCHO$. (d) *$CH_2OHCHOH$. (e) *CH_2OHCHO. (f) *CH_2OH. (g) *CH_2O. (h) *CHO. (i) *HCOOH.

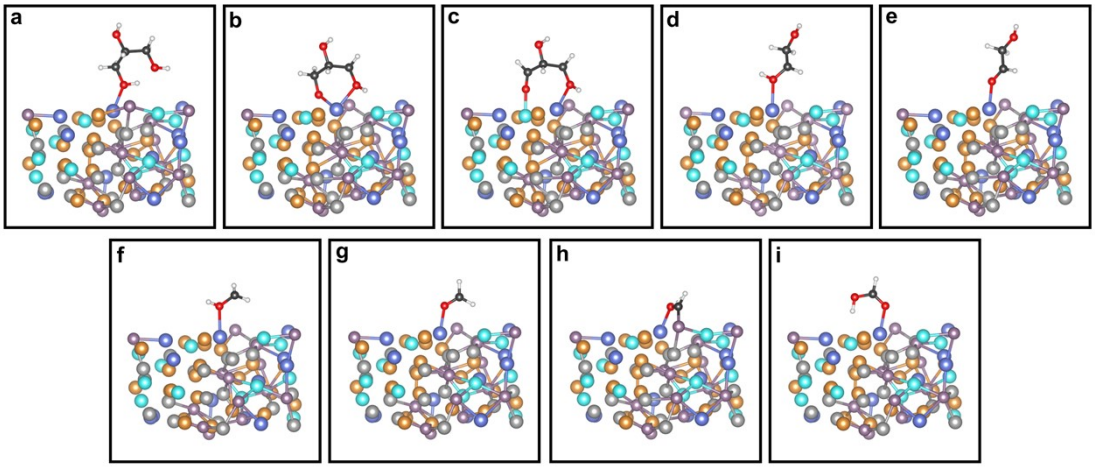

Fig. S40. Optimized structure models of FeCoNiCuP absorbed with different intermediates on Cu site. (a) *$CH_2OHCHOHCH_2OH$. (b) *$CH_2OHCHOHCH_2O$. (c) *$CH_2OHCHOHCHO$. (d) *$CH_2OHCHOH$. (e) *CH_2OHCHO. (f) *CH_2OH. (g) *CH_2O. (h) *CHO. (i) *HCOOH.

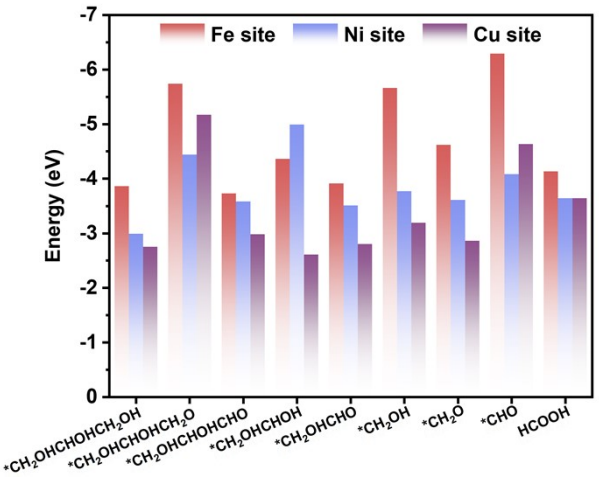

Fig. S41. Adsorption energies of intermediates on Fe, Ni and Cu sites.

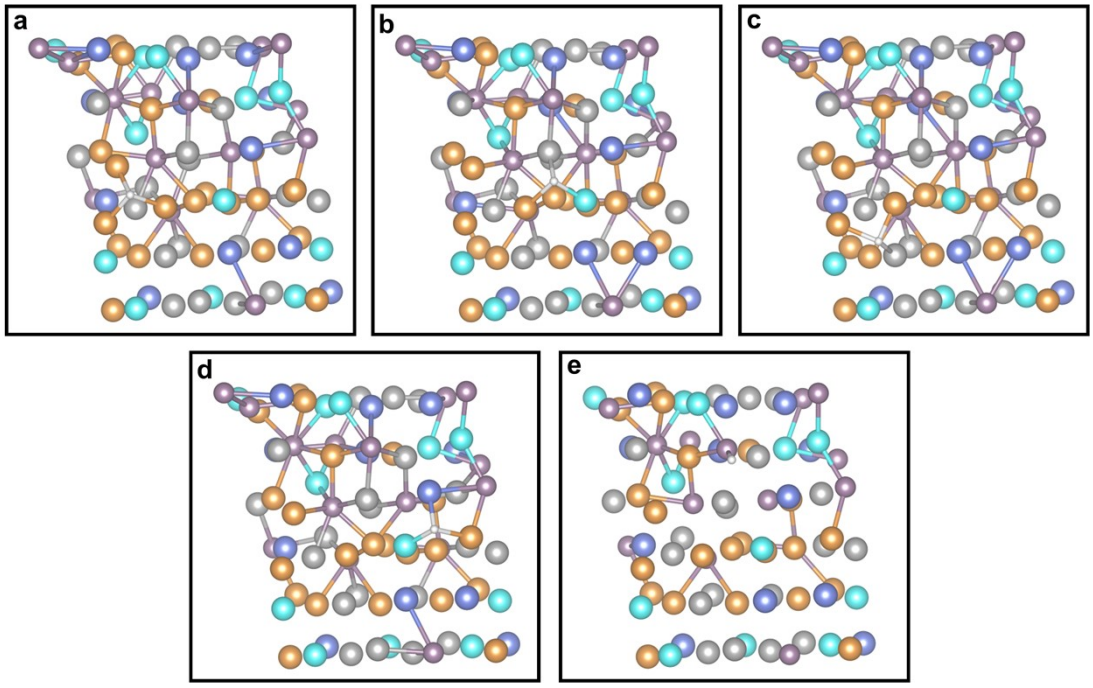

Fig. S42. Optimized structure models of FeCoNiCuP adsorbed with *H on different sites. (a) Fe site, (b) Co site, (c) Ni site, (d) Cu site, (e) P site.

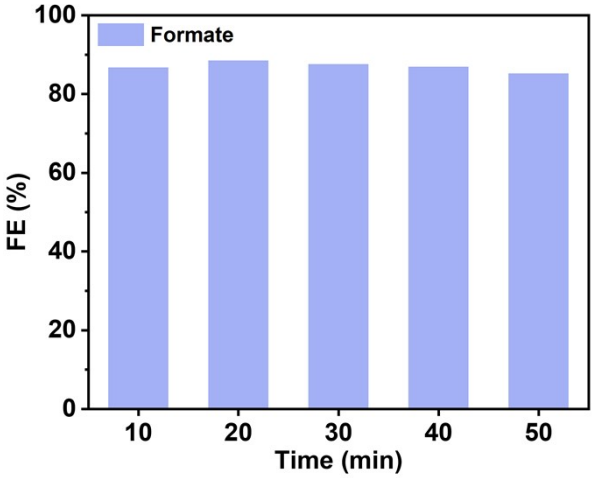

Fig. S43. The FE of formate in GOR-coupled electrolyzer.

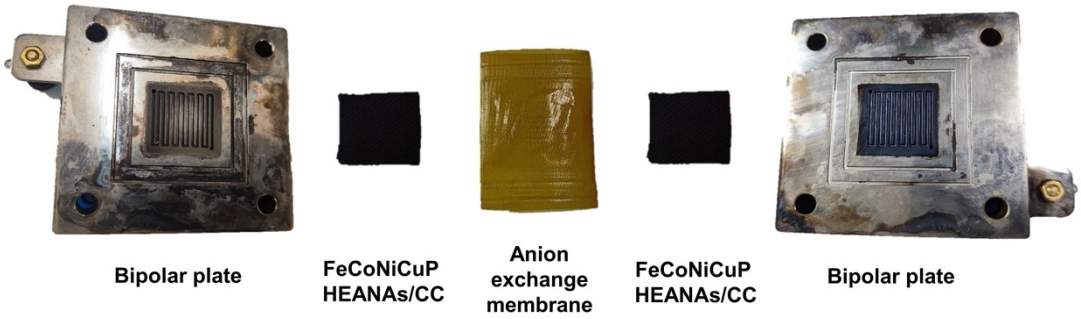

Fig. S44. Photograph of the components of the electrochemical reactor.

Fig. S45. Photograph of the electrochemical setup with continuous mode.

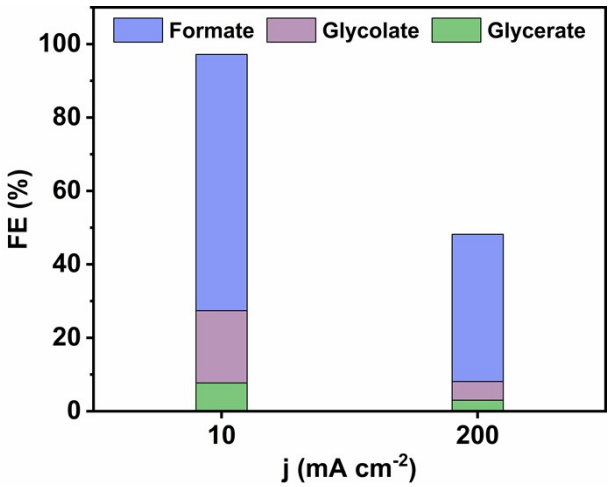

Fig. S46. The FEs of glycerate, glycolate, and formate in the electrochemical setup with continuous mode at the current densities of 10 mA cm^{-2} and 200 mA cm^{-2}.

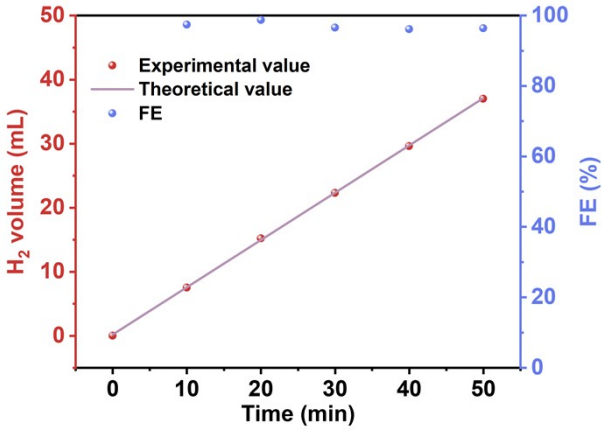

Fig. S47. The FE of H_2 in GOR-coupled seawater electrolyzer.

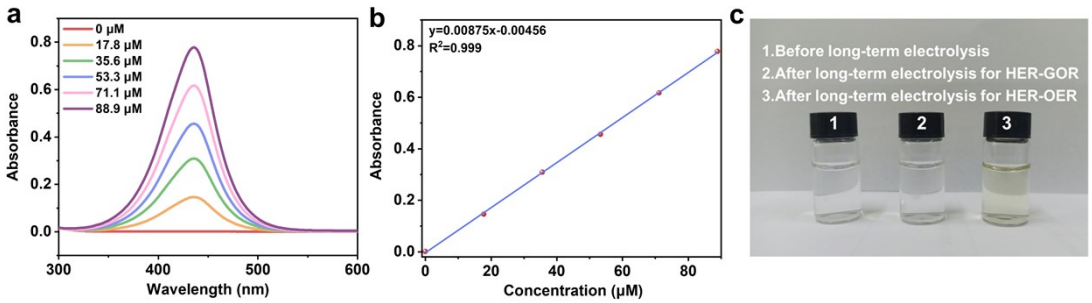

Fig. S48. (a) UV-vis absorption spectra of the solutions containing 0.5 mL o-tolidine with different concentrations of hypochlorite. (b) The standard curve obtained by plotting the hypochlorite concentration against absorption peak intensity at λ = 436 nm. (c) The optical images of the extracted electrolyte from different electrolysis conditions. The o-tolidine is used as a color reagent to detect the presence of pypocholoride, and solution containing pypocholoride turns yellow.

Supplementary Tables

Table S1. The ICP-AES results of FeCoNiCuP HEANAs.

Elements	at%
Fe	30.3
Co	16.9
Ni	23.5
Cu	12.9
P	16.4

Table S2. The EDS results of FeCoNiCuP samples with different proportions.

	Fe (at%)	Co (at%)	Ni (at%)	Cu (at%)	P (at%)
FeCoNiCuP HEANAs	**27.9**	**15.5**	**24.9**	**14.4**	**17.3**
FeCoNiCuP-2	11.3	31.4	29.7	14.2	13.4
FeCoNiCuP-3	8.4	33.5	29.9	9.0	19.2
FeCoNiCuP-4	3.5	42.3	28.5	10.7	15.0
FeCoNiCuP-5	29.5	38.3	17.7	3.7	10.8

Table S3. Comparison of the FeCoNiCuP HEANAs catalyst with the reported catalysts for organic molecules oxidation assisted H_2 production.

Catalyst	Electrolyte	E_{OER} (V)	E_{OOR} (V)	ΔE (mV)	E_1 (V)	E_2 (V)	Reference
FeCoNiCuP HEANAs	**1 M KOH + 0.1 M glycerol**	**1.49**	**1.28**	**210**	**1.61**	**1.40**	**This work**
CoO	1 M KOH + 0.1 M glycerol	1.53	1.32	210	-	-	7
CoO_x/MWCNTs-O_x	1 M KOH + 1 M glycerol	1.62	1.49	130	-	-	8
$Co(OH)_2$@HOS	1 M KOH + 3 M methanol	1.57	1.39	180	1.63	1.50	9
NiSe@NiO_x	1 M KOH + 10 mM HMF	1.55 (onset)	1.35 (onset)	200	1.70 (onset)	1.50 (onset)	10
Ni_2P	1 M KOH + 0.5 mmol THIQs	1.48 (onset)	1.32 (onset)	160	-	-	11
CoNiCuMnMo-NPs	1 M KOH + 0.1 M glycerol	1.55	1.25	300	1.63	1.34	12
Ni-Mo-N	1 M KOH + 0.1 M glycerol	1.57	1.30	270	1.62	1.36	13
$Rh_{0.3}\{Ni(OH)_2\}_{0.7}$/C	1 M KOH + 0.5 M glycerol	1.456	1.29	166	-	-	14
Mo-Ni	1 M KOH + 10 mM benzyl alcohol	1.49	1.345	145	1.49	1.38	15
Ni_2P-UNMs	1 M KOH + 0.125 M benzylamine	1.52	1.34	180	1.53	1.41	16

All potentials are referenced to RHE. All potentials are listed at 10 mA cm^{-2} unless otherwise marked. E_{OER}: potential for OER. E_{OOR}: potential for the oxidation of organic molecules. $\Delta E = E_{OER} - E_{OOR}$. E_1: cell voltage for traditional electrolyzer. E_2: cell voltage for organic molecule oxidation assisted electrolyzer. “Onset” means the onset potential.

References

1 G. Wang and Z. Wen, *Nanoscale*, 2018, **10**, 21087-21095.

2 J. P. Perdew, K. Burke and M. Ernzerhof, *Phys. Rev. Lett.*, 1996, **77**, 3865-3868.

3 G. Kresse and D. Joubert, *Phys. Rev. B*, 1999, **59**, 1758-1775.

4 A. van de Walle, *Calphad*, 2009, **33**, 266-278.

5 A. van de Walle, M. Asta and G. Ceder, *Calphad*, 2002, **26**, 539-553.

6 A. van de Walle, P. Tiwary, M. de Jong, D. L. Olmsted, M. Asta, A. Dick, D. Shin, Y. Wang, L. Q. Chen and Z. K. Liu, *Calphad*, 2013, **42**, 13-18.

7 N. Xi, Y. Zang, X. Sun, J. Yu, M. Johnsson, Y. Dai, Y. Sang, H. Liu and X. Yu, *Adv. Energy Mater.*, 2023, **13**, 2301572.

8 D. M. Morales, D. Jambrec, M. A. Kazakova, M. Braun, N. Sikdar, A. Koul, A. C. Brix, S. Seisel, C. Andronescu and W. Schuhmann, *ACS Catal.*, 2022, **12**, 982-992.

9 K. Xiang, D. Wu, X. Deng, M. Li, S. Chen, P. Hao, X. Guo, J.-L. Luo and X.-Z. Fu, *Adv. Funct. Mater.*, 2020, **30**, 1909610.

10 L. Gao, Z. Liu, J. Ma, L. Zhong, Z. Song, J. Xu, S. Gan, D. Han and L. Niu, *Appl. Catal. B Environ.*, 2020, **261**, 118235.

11 C. Huang, Y. Huang, C. Liu, Y. Yu and B. Zhang, *Angew. Chem. Int. Ed.*, 2019, **58**, 12014-12017.

12 L. Fan, Y. Ji, G. Wang, J. Chen, K. Chen, X. Liu and Z. Wen, *J. Am. Chem. Soc.*, 2022, **144**, 7224-7235.

13 Y. Li, X. Wei, L. Chen, J. Shi and M. He, *Nat. Commun.*, 2019, **10**, 5335.

14 F. F. S. Xavier, A. C. Cunha, T. W. Napporn and P. Olivi, *Int. J. Hydrogen Energy*, 2023, **48**, 31091-31100.

15 X. Cui, M. Chen, R. Xiong, J. Sun, X. Liu and B. Geng, *J. Mater. Chem. A*, 2019, **7**, 16501-16507.

16 Y. Ding, B.-Q. Miao, S.-N. Li, Y.-C. Jiang, Y.-Y. Liu, H.-C. Yao and Y. Chen, *Appl. Catal. B Environ.*, 2020, **268**, 118393.